Materials Science & Engineering A 831 (2022) 142271

Contents lists available at ScienceDirect

Materials Science & Engineering A

journal homepage: www.elsevier.com/locate/msea

Secondary phases strengthening-toughening effects in the Mo–TiC–La_2O_3 alloys

Bo-Liang Hu [a,b], Jia-Yu Han [a,b], Song-Wei Ge [a,b], Xing-Jiang Hua [a,b], Shi-Lei Li [a,b], Hai-Rui Xing [a,b], Kuai-She Wang [a,b,**], Ping Hu [a,b,*], Jing-Bo Fu [c], Wen Zhang [d], Alex A. Volinsky [e,f], Ekaterina S. Marchenko [f]

[a] School of Metallurgy Engineering, Xi'an University of Architecture and Technology, Xi'an, 710055, China
[b] National and Local Joint Engineering Research Functional Center for Materials Processing, Xi'an University of Architecture and Technology, Xi'an, 710055, China
[c] Jinduicheng Molybdenum Co., Ltd., Xi'an, 710077, China
[d] Northwest Institute for Non-ferrous Metal Research, Xi'an, 710016, China
[e] Department of Mechanical Engineering, University of South Florida, Tampa, FL, 33620, USA
[f] Laboratory of Superelastic Biointerfaces, Tomsk State University, 36 Lenin Ave., Tomsk, 634050, Russian Federation

ARTICLE INFO

Keywords:
Mo-TiC-La_2O_3 alloy
Secondary phase
Mismatch
Interface
Strengthening-toughening

ABSTRACT

Mo–TiC–La_2O_3 molybdenum alloys were strengthened and toughened by the synergistic action of nano-carbide particles and rare earth oxides. In this paper, the Mo–TiC–La_2O_3 alloy system was prepared by powder metallurgy. The microstructure was characterized by optical, scanning, and transmission electron microscopy. The mechanical properties were tested using the hardness tester and universal tensile testing machine. The grain size of the Mo–TiC–La_2O_3 alloy is smaller than the Mo–TiC and Mo–La_2O_3 alloys. The strength and elongation of annealed Mo–TiC–La_2O_3 alloy are 1291 MPa and 6.6%, respectively. The strength and ductility of the annealed Mo–TiC–La_2O_3 alloy are higher than the Mo–TiC and Mo–La_2O_3 alloys. According to the interfacial mismatch between the secondary phases and the matrix, along with oxygen impurities interactions, the mechanisms of strengthening and toughening of the secondary phases in the Mo–TiC–La_2O_3 alloy were revealed.

1. Introduction

Pure molybdenum has no phase transitions, so the secondary phases play a major role in its strengthening and toughening. The strength and ductility of the Mo–TiC–La_2O_3 alloy were improved by doping rare earth and ceramic particles. The addition of the carbide phase to the TZM alloys can promote the formation of dimples during the high-temperature deformation process, and transform the high temperature mixed fracture of transgranular cleavage and dimples to the single dimple fracture, which can improve high-temperature strength and plasticity [1]. However, high-temperature oxidation resistance and comprehensive mechanical properties are seriously degraded by partial enrichment with graphite carbon [2]. Many researchers improved the strength and toughness of molybdenum alloys through particle refinement, spheroidization and homogenization of secondary phases, and prepared Al_2O_3 dispersed-strengthened molybdenum alloys [3], WO_X nanomaterials [4], and Mo–Cu composite powders with core-shell structure [5] by the hydrothermal method, solution combustion synthesis, and heterogeneous precipitation, respectively. Therefore, refining and homogenizing secondary phases are important methods for preparing dispersed-strengthened high-performance molybdenum alloys [6,7]. In addition, molybdenum alloys' properties can be improved by multi-component alloying.

Mo–La–Y, Mo–La–Ce, Mo–Y–Ce, Mo–La–Ce–Y, and Mo–La–Ce–Y alloys were designed. The composite rare earth elements can effectively refine the grain size down to 1.3–2.4 μm. The oxide particle size of the two-component and three-component alloys ranges from 73 nm to 105 nm. With the rare earth elements addition, dislocations bend in an arch between the oxide particles, and the particles pin dislocations. With the increase of stress, the dislocations will pass through the oxide particles and produce dislocation rings in the multi-component oxides-doped molybdenum alloys [8]. For the multi-component rare earth elements

* Corresponding author. School of Metallurgy Engineering, Xi'an University of Architecture and Technology, Xi'an, 710055, China.
** Corresponding author. National and Local Joint Engineering Research Functional Center for Materials Processing, Xi'an University of Architecture and Technology, Xi'an, 710055, China.
E-mail addresses: wangkuaishe888@126.com (K.-S. Wang), huping1985@126.com (P. Hu).

https://doi.org/10.1016/j.msea.2021.142271
Received 3 August 2021; Received in revised form 25 October 2021; Accepted 28 October 2021
Available online 2 November 2021

and carbides composite Mo–La_2O_3–ZrC alloy, nano-sized La_2O_3 and ZrC particles are dispersed intragranular and at grain boundaries, and dislocations are pinned around these particles. The optimal combination of strength and ductility allows the ultimate tensile strength to reach 988 MPa and the total elongation to reach 10% at 25 °C [9].

The strength and toughness of the Mo–TiC–La_2O_3 alloy depend on the TiC and La_2O_3 phases, along with other composite phases. However, the strengthening mechanism and the action of secondary phases in the Mo–TiC–La_2O_3 alloy relative to Mo–TiC and Mo–La_2O_3 alloys have not been analyzed yet. In this paper, Mo–TiC, Mo–La_2O_3, and Mo–TiC–La_2O_3 molybdenum alloys with different compositions were prepared by solid-liquid doping. The effects of different secondary phases on the microstructure, strength, and plasticity relative to the Mo–TiC and Mo–La_2O_3 alloys were studied after deformation and annealing.

2. Experimental procedure

Table 1 shows three molybdenum alloys with different components, based on the Mo–TiC–La_2O_3 alloy system, including Mo–La_2O_3, Mo–TiC, and Mo–TiC–La_2O_3 alloys. The organic carbon source exists in every alloy, and its composition and content are the same as in the Mo–TiC–La_2O_3 alloy. The starting materials included high-purity molybdenum powder (Jinduicheng Molybdenum Co., Ltd.), fructose ($\mathbf{C_6H_{12}O_6}$) (Xi'an Shuangde Biotechnology Co., Ltd.), nano-TiC (China General Research Institute of Metal Powder), and rare earth La $(NO_3)_3$•$6H_2O$ (Tianjin Guangfu Fine Chemical Research Institute).

As shown in Fig. 1, the preparation process includes powder mixing, vacuum drying, ball milling, cold isostatic pressing, hydrogen sintering, rolling, and hydrogen annealing. According to the composition listed in Table 1, the molybdenum powder was mixed with nano-TiC in a three-dimensional mixer for 120 min. Then, $C_6H_{12}O_6$ and $La(NO_3)_3{\cdot}6H_2O$ dissolved in distilled water were added to the molybdenum powder. After the mixture was uniform, the solution was aged for 2 h and dried in a vacuum oven at 80 °C for 4 h. Then, after cooling to room temperature in the furnace, the dried alloy powder was placed into the ball-milling tank with the ball:material ratio of 2:1 and ground for 2 h with a planetary ball mill. The alloy powders were pressed at 180 MPa for 10 min with a cold isostatic press and then sintered at 1920 °C in hydrogen. The sintered samples were hot-rolled, warm rolled and cold rolled to 0.5 mm plate, respectively. At last, some samples were annealed at 950 °C for 1 h.

The microstructure, fracture, and dislocations configuration were characterized by optical microscopy (OM), scanning electron microscopy (SEM), and transmission electron microscopy (TEM). The microhardness of the samples was tested by the 401MVD digital micro Vickers hardness tester with 200 g weight for 15 s. Tensile tests were carried out using Instron 8801 fatigue tester with a tensile speed of 0.5 mm/min. Tensile test samples were prepared according to the ASTM E8.

3. Results and discussion

3.1. Secondary phases effects on microstructure

Fig. 2 shows the metallographic structure of the sintered Mo–TiC–La_2O_3 alloy with different components, and the grain size of the Mo–La_2O_3 alloy is 32.3 ± 4 μm in Fig. 2a. The grain size of the Mo–TiC alloy is 28.9 ± 0.4 μm in Fig. 2c. The size of the secondary phases is at the nanoscale and is difficult to be observed in the metallographic diagram. However, the grain size of the Mo–TiC–La_2O_3 alloy is 27.5 ± 0.8 μm in Fig. 2e, and the secondary phase particles with the size of 1–3 μm are uniformly distributed.

Table 1
Designed composition of the Mo/TiC/La_2O_3 alloy system (wt. %).

Sample	Fructose ($C_6H_{12}O_6$)	TiC	$La(NO_3)_3$•$6H_2O$	Mo
Mo–La_2O_3	0.12	0	3.117	Bal.
Mo–TiC	0.12	0.63	0	Bal.
Mo–TiC–La_2O_3	0.12	0.63	3.117	Bal.

The fracture surfaces of the sintered billet of the three molybdenum alloys are also shown in Fig. 2. The Mo–La_2O_3, Mo–TiC, and composite Mo–TiC–La_2O_3 alloys exhibit intergranular and transgranular fracture. By counting the number of holes in the three alloy billets, the number of pores in the Mo–TiC and Mo–TiC–La_2O_3 alloys is greater than in the Mo–La_2O_3 alloy. The energy spectrum of the secondary phase in Mo–La_2O_3 alloy shows that it contains C, La, O and Mo elements (Fig. 2b). Mo–TiC alloy shows that it contains Ti and Mo elements (Fig. 2d). Mo–TiC–La_2O_3 alloy shows that it contains O, Ti, La and Mo elements (Fig. 2f).

Fig. 3 shows the microstructure after rolling into sheets and annealing at 950 °C. The microstructure of all rolled and annealed alloys is fibrous. After annealing, the microstructure and the secondary phase particles are coarsened in Fig. 3a_2. Whirl structure is visible in the Mo–TiC microstructure in Fig. 3b_2. which often appears in explosive composites. Also appeared in the welding of dissimilar materials. This is an uneven change behavior of the material structure, which does not appear in the rolled structure, but only appears in the Mo–TiC annealed structure. This structure is inevitable related to the grain coarsening of the material. In terms of performance, this uneven structure leads to a low elongation rate of the material, which is prone to uneven deformation, forming cracks, and leading to fractures.

The annealed microstructure of the Mo–La_2O_3 and Mo–TiC alloys shows obvious grain coarsening, while the annealed microstructure of the Mo–TiC–La_2O_3 does not show obvious changes in Fig. 3e_1, e_2. The formation of a variety of secondary phases has an important effect on the microstructure during annealing.

Fig. 4 shows the TEM images and SAD of the molybdenum alloy rolled sheet with different components. The size of the secondary phase nanoparticles is about 52 nm in the Mo–La_2O_3 alloy in Fig. 4a_1 and a_2. However, there is a small amount of the La_2O_3 secondary phase in the alloy which identified by SAD in TEM analysis(4a_2). In the Mo–TiC alloy, the added amount of TiC is 0.63 wt %, and the lamella phases are distributed uniformly in the matrix in Fig. 4b_1. It is mostly distributed in the grain, and the lamella is identified as TiO_2 by SAD and the size is about 60 nm in Fig. 4b_2. The addition amount of TiC and La_2O_3 in the Mo–TiC–La_2O_3 alloy is the same as in the Mo–La_2O_3 and Mo–TiC alloys, and there are both nano and micro-phase particles in the alloy. The size of the nanoparticles is about 60 nm in Fig. 4c_1, and the larger senondary phase is identified as $La_2Ti_2O_7$ and size is 200 nm in Fig. 4c_2.

The volume fraction of the secondary phase in the Mo–La_2O_3 alloy is lower than in the Mo–TiC alloy. The volume fraction of nano-carbide directly added by TiC in the Mo–TiC alloy is significantly higher than in the Mo–TiC–La_2O_3 alloy. In the Mo–TiC–La_2O_3 alloy, lamella TiC does not appear. Large size $La_2Ti_2O_7$ is the main secondary phase in the Mo–TiC–La_2O_3 alloy, so lamella TiC is mostly consumed by reactions with other alloying elements.

When rare earth elements are present in the matrix, the size of the secondary phase is small, consisting mainly of La_2O_3 nanoparticles. In the Mo–TiC–La_2O_3 alloy, rare earth oxides have a special electronic structure when there are many oxides, including La_2O_3. When rare earth elements change from metals to ions, besides losing 6s electrons, 5 d and 4f orbitals also lose an electron, forming$4f^n5s^25p^8$ electron arrangement, and the electron layer is still surrounded by the outer side of the 4f orbital. The electronic structure of rare earth oxides is easily combined with other secondary phases to form a composite phase. Rare earth oxide particles act as the core and other oxides are coated to form a composite phase. Therefore, the components with multiple rare earth elements all have micron-scale granular phases seen in Fig. 4c_1 and 4c_2. The $La_2Ti_2O_7$ composite phase is dispersed in the deformation process.

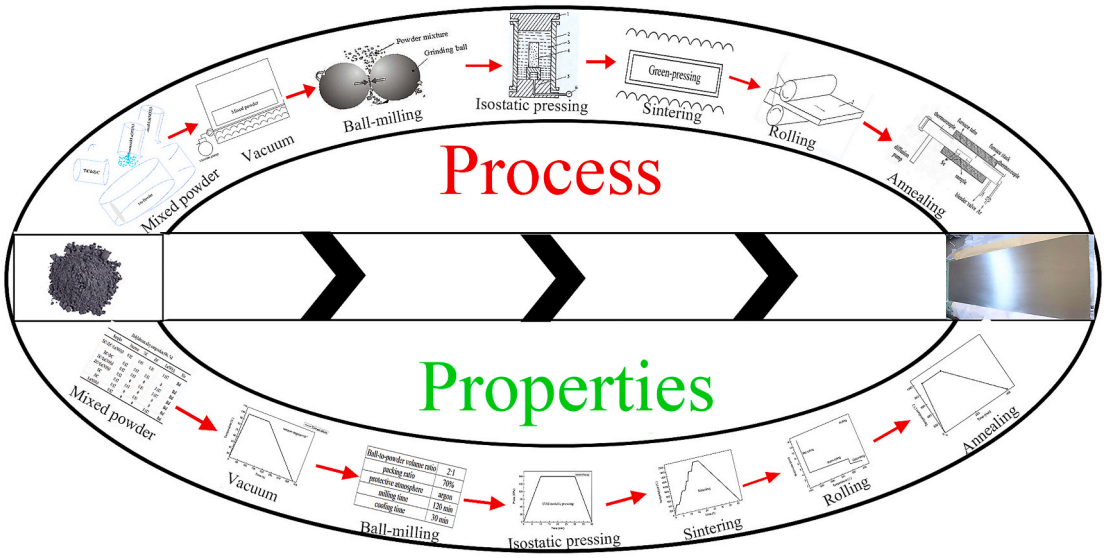

Fig. 1. The preparation process and properties of the Mo–TiC–La_2O_3 alloys.

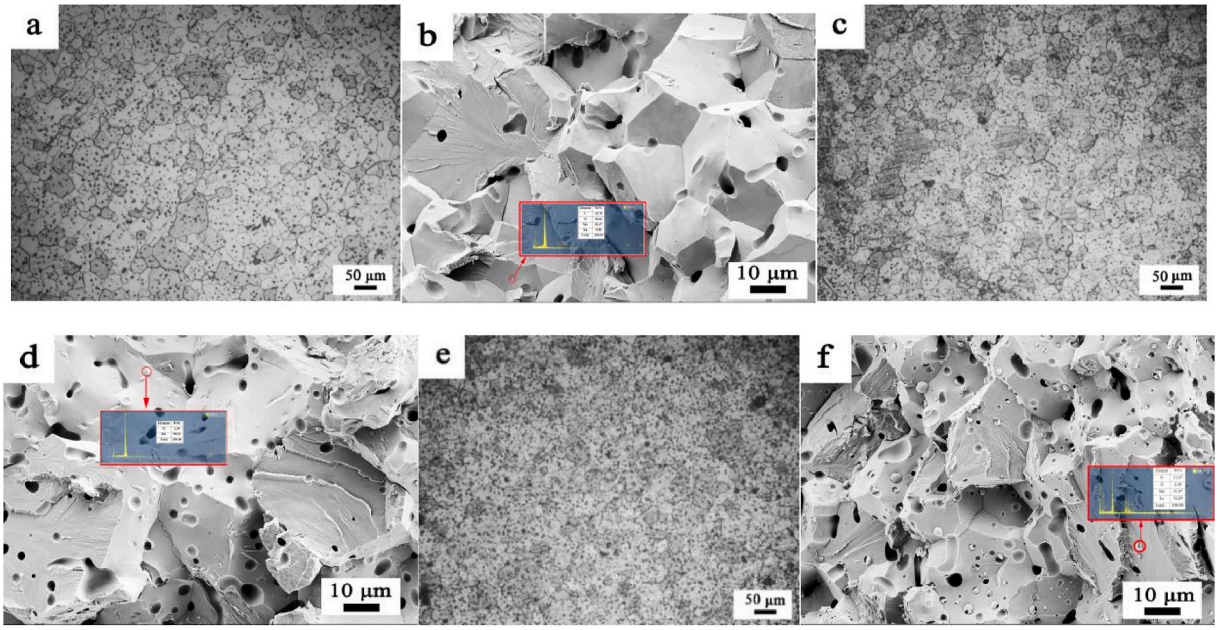

Fig. 2. Microstructure and fracture morphology of nano-TiC doped Mo–TiC–La_2O_3 sintered alloy: (a, b) Mo–La_2O_3; (c, d) Mo–TiC; (e, f) Mo–TiC–La_2O_3.

3.2. Secondary phases effects on mechanical properties

3.2.1. Hardness

Fig. 5 shows the hardness with different components of molybdenum alloy in the sintered state, after rolling and annealing at 950 °C. In the sintered state, Mo–La_2O_3 alloy has a hardness of 146 ± 9.08 HV, Mo–TiC alloy is 158.8 ± 8.28 HV and Mo–TiC–La_2O_3 alloy is 154.1 ± 8.17 HV. In the sintered billet, the volume fraction of the secondary phases in the Mo–TiC alloy is higher, so the hardness is higher. The large size of the secondary phases in the Mo–TiC–La_2O_3 alloy makes the hardness higher than the nano-phase Mo–La_2O_3 alloy.

The hardness of the Mo–La_2O_3 rolled samples is 338.25 ± 13.56 HV, Mo–TiC is 414.44 ± 16.98 HV, and Mo–TiC–La_2O_3 is 368.1 ± 146 HV. After annealing at 950 °C, the hardness of the Mo–La_2O_3 alloy is 264.75 ± 11.88 HV, Mo–TiC alloy is 362.23 ± 36.1 HV, and Mo–TiC–La_2O_3 alloy is 351.65 ± 198 HV. The hardness of the rolled state is higher than the annealed state. The highest hardness is obtained in the Mo–TiC alloy in both rolled and annealed states. However, the Mo–La_2O_3 alloy has the lowest hardness after rolling and annealing.

The hardness varies with the composition of the alloy. Specific manifestations are as follows. After annealing at 950 °C, the hardness of the Mo–La_2O_3 alloy decreases by 21.7%, Mo–TiC decreases by 12.6%, and Mo–TiC–La_2O_3 decreases by 4.5%. The hardness of Mo–TiC–La_2O_3 alloy decreases the least. The main reason is that there are $La_2Ti_2O_7$ and nano phases in the Mo–TiC–La_2O_3 alloy, which can effectively hinder the softening of dislocations in the recovery process. The Mo–TiC hardness decrease is lower than Mo–La_2O_3, mainly because the TiC phase exists in the lamella form, and the hindering effect on dislocations is greater. The hardness of the Mo–La_2O_3 alloy decreases due to only a small amount of the La_2O_3 phase in the Mo–La_2O_3 alloy, which cannot effectively hinder the softening of dislocations in the recovery process.

3.2.2. Tensile mechanical properties

Fig. 6 shows tensile stress-strain curves of different molybdenum

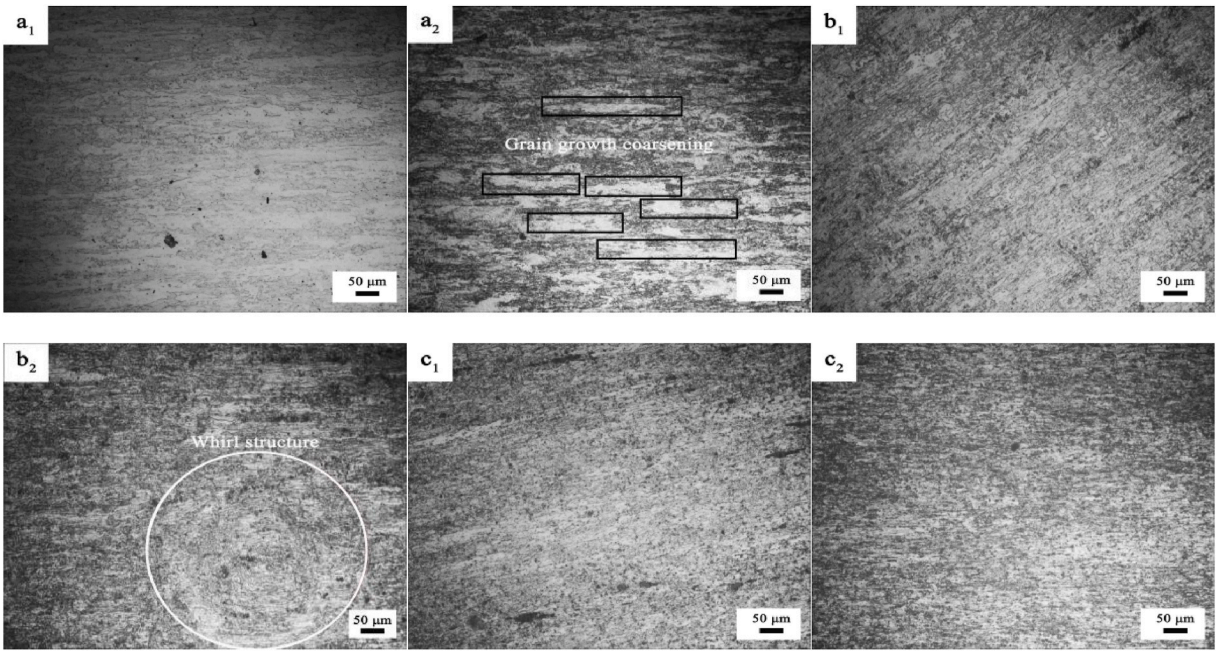

Fig. 3. Microstructure of the Mo–TiC–La_2O_3 alloys:
(a_1) Mo–La_2O_3; (a_2) Mo–La_2O_3 annealed at 950 °C; (b_1) Mo–TiC; (b_2) Mo–TiC annealed at 950 °C; (c_1) Mo–TiC–La_2O_3, (c_2) Mo–TiC–La_2O_3 annealed at 950 °C.

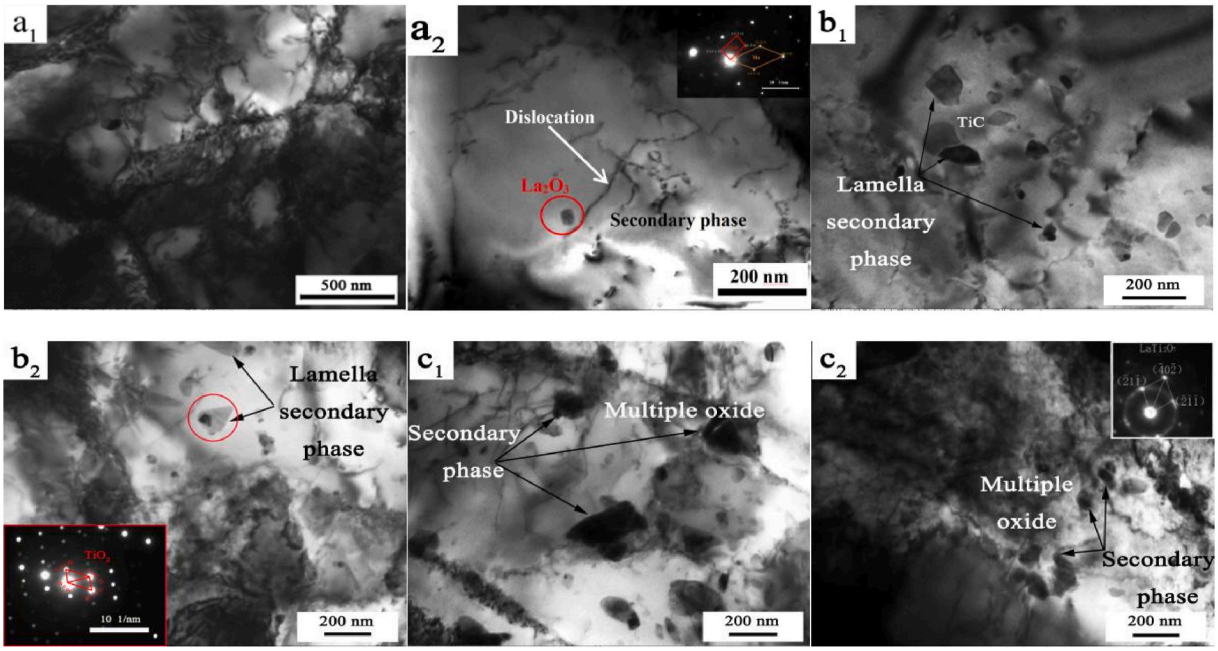

Fig. 4. TEM images of the Mo–TiC–La_2O_3 alloys plate:
(a_1, a_2) Mo–La_2O_3; (b_1, b_2) Mo–TiC; (c_1, c_2) Mo–TiC–La_2O_3.

alloys after rolling and annealing at 950 °C. The mechanical properties of the samples are as follows. Mo–La_2O_3 alloy has 898.14 MPa tensile strength and 9.91% elongation, Mo–TiC alloy has 1240.23 MPa tensile strength, and 5.3% elongation, Mo–TiC–La_2O_3 alloy has 1291.68 MPa tensile strength and 6.59% elongation. As seen in Fig. 6a and b, the strength of Mo–TiC increases compared with the Mo–La_2O_3 alloy. The addition of TiC significantly improves the tensile strength of molybdenum alloy compared with La_2O_3, but it also significantly reduces the elongation. Compared with the Mo–La_2O_3 alloy, the tensile strength of Mo–TiC–La_2O_3 increases by 43.82% and the elongation decreases by 33.5%. Compared with the Mo–TiC alloy, the tensile strength, and elongation of the Mo–TiC alloy increase by 4.2% and 19%.

The bar chart in Fig. 6c shows the product of the tensile strength and elongation in the rolled and annealed states, representing the comprehensive effect of strengthening and toughening. The annealed state properties of the same composition alloy are greater than the rolled state. Therefore, Mo–TiC–La_2O_3 has optimal comprehensive properties of the three molybdenum alloys (1291.68 MPa tensile strength and 6.59% elongation).

3.2.3. *Strengthening and toughening mechanisms*

According to the Ashby-Orowan equation [12]:

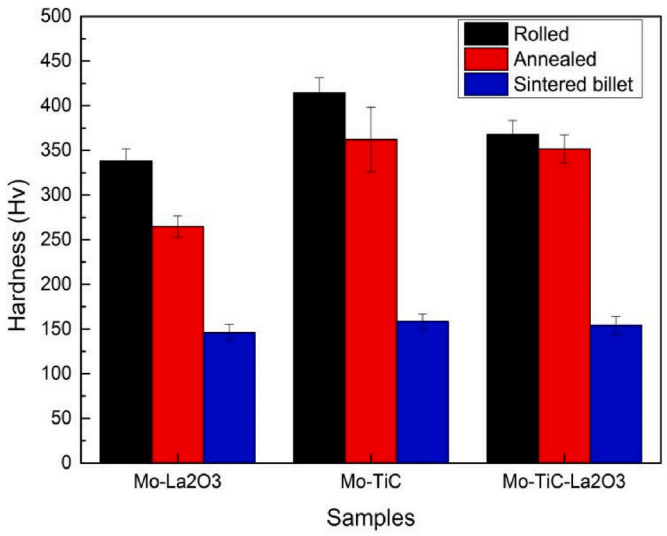

Fig. 5. The hardness of TiC/La_2O_3 doped Mo–TiC–La_2O_3 alloy system (sintered billet, rolled and 950 °C annealed).

$$\sigma_p = \frac{m\mu b}{1.18 \times 2\pi r\left(\sqrt{\frac{\pi}{6f_v}} - 1\right)} \ln\left(\frac{r}{2b}\right) \tag{1}$$

Here, m is the Taylor factor, μ is the shear modulus, b is the Burgers vector, r is particle size, and f_V is particle volume fraction. Based on this equation, the decrease of particle size and the increase of particle volume will increase the strength of the material.

The secondary phases in Mo–La_2O_3 and Mo–TiC alloys are mainly of nanometer size, and the volume fraction in Mo–TiC is much higher than in the Mo–La_2O_3 alloy, so the strength of the alloy is higher than the Mo–La_2O_3 alloy. In the Mo–TiC–La_2O_3 alloy, there are not only nanoscale but also microscale secondary phases. The volume fraction of the secondary phases is higher than Mo–La_2O_3 and Mo–TiC alloys, and the strength is the highest.

The precipitation of particles with slight mismatches in the matrix will produce a stress field, which hinders the movement of dislocations. For the dislocation to pass through the internal stress region, the applied stress must be at least equal to the average internal stress. For spherical and small coherent particles, the flow stress is determined as:

$$\tau = 4.1\mu\varepsilon^{2/3} f^{1/2} (r/b)^{1/2} \tag{2}$$

For large mismatched particles, the strengthening effect can be predicted as [10]:

$$\tau = 0.7\mu f^{1/2} \left(\varepsilon b^3 / r^3\right)^{1/4} \tag{3}$$

Here, μ is the shear modulus, ε is the mismatch of particles with the matrix, f is the precipitated phase volume fraction. Regardless of the particle size, the strengthening phase mismatch is proportional to the stress, and a large mismatch will produce greater distortion stress in the surrounding and reinforcement matrix. The smaller mismatch corresponds to lower distortion stress, and the corresponding reinforcement is reduced.

The main secondary phase in the Mo–La_2O_3 alloy is La_2O_3, as shown in Fig. 7a. The phase relations between the La_2O_3 and Mo secondary phase in the body-centered cubic structure on planes (100), (110), and (111) are calculated in Table 2. Its low index crystal plane $(100)_{La2O3}//(100)_{Mo}$ mismatches 28.83%, belonging to the non-coherent interface, $(110)_{La2O3}//(110)_{Mo}$ mismatches 16.15%, and $(111)_{La2O3}//(111)_{Mo}$ mismatches 10.64%, both belonging to the semi-coherent interface.

The phase relations between the secondary TiC and Mo phases on the (100), (110), and (111) planes are shown in Fig. 7b. The calculated

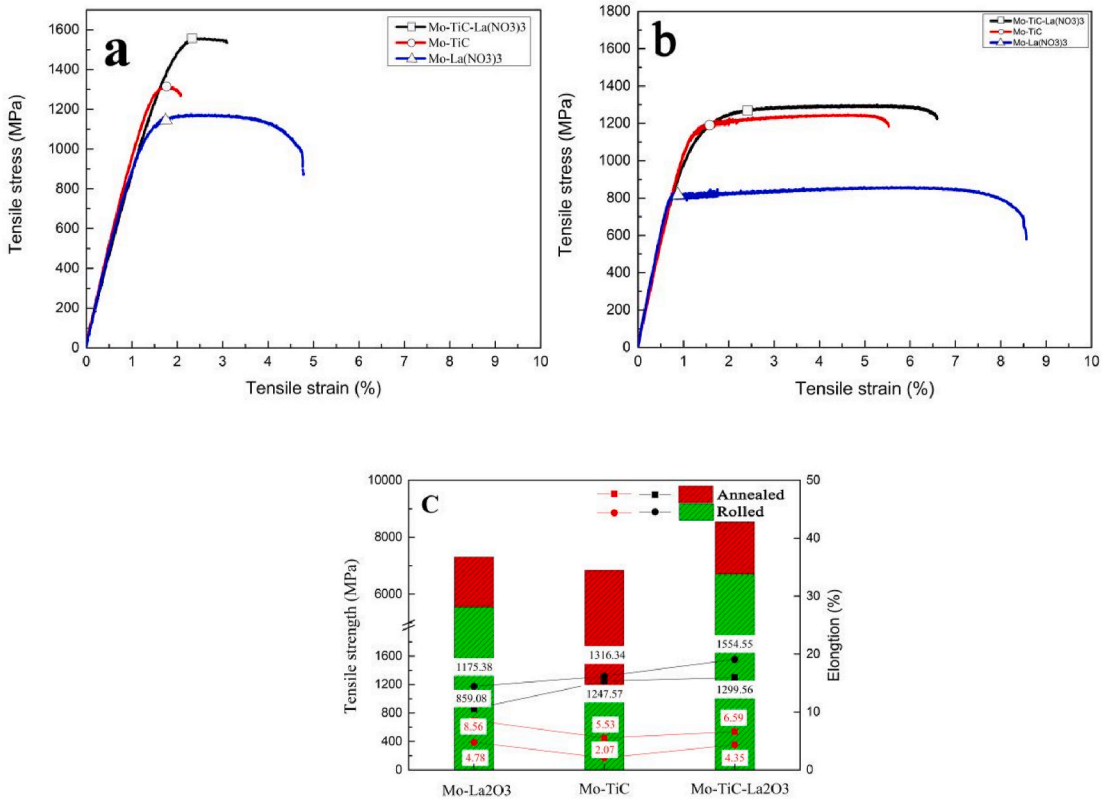

Fig. 6. Tensile properties of nanometer TiC/La_2O_3 doped Mo alloy system in rolled and annealing states: (a) engineering stress-strain curves of rolled alloys; (b) engineering stress-strain curves of annealed alloys; (c) strength and elongation in annealed and rolled states.

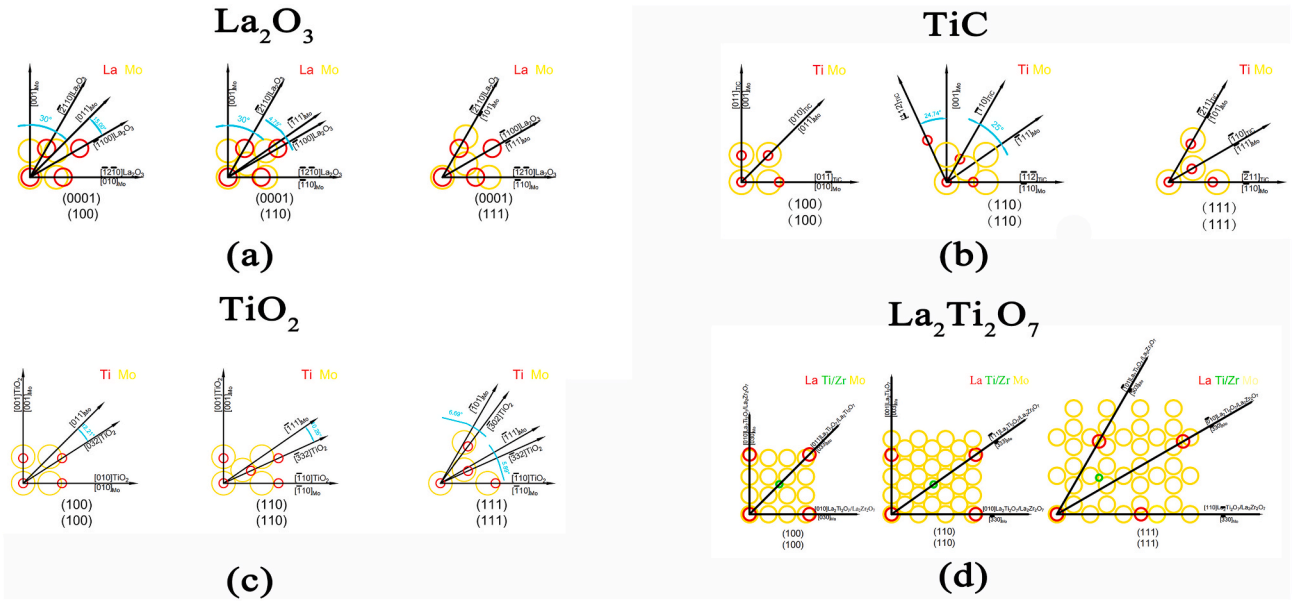

Fig. 7. The phase relationships between La_2O_3, TiC, TiO_2, $La_2Ti_2O_7$, and Mo on low index surfaces.

Table 2
Mismatch calculated values of La_2O_3 (Im-3m) and Mo lattice.

Content	Matching interface								
	(100) La_2O_3// (100) $_{Mo}$			(110) La_2O_3// (110) $_{Mo}$			(111) La_2O_3// (111) $_{Mo}$		
[*uvw*]La_2O_3	[010]	[011]	[001]	[$\bar{1}$11]	[$\bar{1}$11]	[$\bar{1}$11]	[$\bar{1}$11]	[$\bar{1}$11]	[101]
[*uvw*]$_{Mo}$	[010]	[011]	[001]	[$\bar{1}$10]	[$\bar{1}$11]	[001]	[$\bar{1}$10]	[$\bar{1}$11]	[101]
d[*uvw*]La_2O_3, nm	0.44563	0.63022	0.44563	0.38593	0.63346	0.38593	0.63022	0.36386	0.63022
d[*uvw*]$_{Mo}$, nm	0.31715	0.44852	0.31715	0.45715	0.55639	0.31715	0.56316	0.32514	0.56316
θ, °	0	15	30	0	4.75	30	0	0	0
δ	**28.83%**			**16.15%**			**10.64%**		

results are listed in Table 3. In the Mo matrix, the mismatch degree of the low index TiC plane $(100)_{TiC}//(100)_{Mo}$ is 10.82%. The $(110)_{TiC}//(110)_{Mo}$ mismatch is 30.93% and the $(111)_{TiC}//(111)_{Mo}$ mismatch is 8.32%. Fig. 7c shows the phase relations between the secondary TiO_2 and Mo phases on the (100), (110), and (111) planes, and the calculated results are listed in Table 4. The mismatch degree of the low index $(100)_{TiO2}//(100)_{Mo}$ crystal plane in the molybdenum matrix is 18.54%, which belongs to the semi-coherent interface. The $(110)_{TiO2}//(110)_{Mo}$ mismatch is 20.18%, belonging to the semi-coherent interface, and the $(111)_{TiO2}//(111)_{Mo}$ mismatch is 8.7%, belonging to the semi-coherent interface.

Fig. 7 calculates the mismatches between different secondary phases and molybdenum matrix in three kinds of alloys. These mismatches are calculated according to bramfit two-dimensional mismatch theory and low exponential crystal planes are selected to calculate the mismatches. Mo–TiC–La_2O_3 alloy mainly has TiC, TiO_2, La_2O_3 and the generated phase is $La_2Ti_2O_7$. The number of strengthening phases is large and they are evenly distributed. The strengthening phases include lamella TiC, rod-like TiO_2, and spherical $La_2Ti_2O_7$, as shown in Fig. 7d. The phase relations of the secondary $La_2Ti_2O_7$ and Mo phases on the (100), (110), and (111) planes are calculated and listed in Table 5. The mismatch degree of the low index crystal plane $(0001)_{La2Ti2O7}//(100)_{Mo}$ in the Mo matrix is 5.53%, belonging to the semi-coherent interface. The $(0001)_{La2Ti2O7}//(110)_{Mo}$ mismatch is 4.4%, belonging to the coherent interface, and the $(0001)_{La2Ti2O7}//(111)_{Mo}$ mismatch is 14.4%, belonging to the semi-coherent interface.

In Mo–La_2O_3, Mo–TiC, and Mo–TiC–La_2O_3 alloys, there are two cases regarding secondary phases. One is the nanocrystalline phase size and the matrix mismatch is not coherent (semi-coherent or non-coherent), the second case is the nano-micro phase size, and the matrix mismatch is greater than 5%. In these two cases, the grains are equiaxed with uniform size and will not grow abnormally.

For the molybdenum alloy system, the coherent relation can exert the toughening effect in the material, and the low mismatched coherent

Table 3
Mismatch calculated values of TiC and Mo lattice.

Content	Matching interface								
	(100) $_{TiC}$// (100) $_{Mo}$			(110) $_{TiC}$// (110) $_{Mo}$			(111) $_{TiC}$// (111) $_{Mo}$		
[*uvw*]$_{TiC}$	[01$\bar{1}$]	[010]	[011]	[$\bar{1}$12]	[$\bar{1}$10]	[$\bar{1}$12]	[$\bar{2}$11]	[$\bar{1}$10]	[$\bar{2}$11]
[*uvw*]$_{Mo}$	[010]	[011]	[001]	[$\bar{1}$10]	[$\bar{1}$11]	[001]	[$\bar{1}$10]	[$\bar{1}$11]	[101]
d[*uvw*]$_{TiC}$, nm	0.43783	0.43783	0.30959	0.30959	0.30959	0.53623	0.51211	0.30959	0.51211
d[*uvw*]$_{Mo}$, nm	0.31715	0.44852	0.31715	0.45715	0.27820	0.31715	0.56316	0.32514	0.56316
θ, °	0	0	0	25.25	24.74	0	0	0	0
Δ	10.82%			30.93%			8.32%		

Table 4
Mismatch calculated values of TiO_2 and Mo lattice.

Content	Matching interface								
	(100) TiO_2// (100) $_{Mo}$			(110) TiO_2// (110) $_{Mo}$			(111) TiO_2// (111) $_{Mo}$		
[*uvw*]TiO_2	[010]	[032]	[001]	[$\bar{1}$10]	[$\bar{3}$32]	[001]	[$\bar{1}$10]	[$\bar{3}$32]	[$\bar{3}$02]
[*uvw*]$_{Mo}$	[010]	[011]	[001]	[$\bar{1}$10]	[$\bar{1}$11]	[001]	[$\bar{1}$10]	[$\bar{1}$11]	[101]
d[*uvw*]TiO_2, nm	0.44627	0.55223	0.29903	0.65658	0.36073	0.29903	0.65658	0.35965	0.54952
d[*uvw*]$_{Mo}$, nm	0.31715	0.44852	0.31715	0.45715	0.27820	0.31715	0.56316	0.32514	0.56316
θ, °	0	0	0	0	10.26	0	0	5.89	6.69
δ	**18.54%**			**20.18%**			**8.7%**		

Table 5
Mismatch calculated values of the $La_2Ti_2O_7$ and Mo lattice.

Content	Matching interface								
	$(100)_{La2Ti2O7}$//$(100)_{Mo}$			$(110)_{La2Ti2O7}$//$(110)_{Mo}$			$(111)_{La2Ti2O}$//$(111)_{Mo}$		
[*uvw*]$_{La2Ti2O7}$	[010]	[011]	[010]	[001]	[$\bar{1}$11]	[001]	[[$\bar{1}$10]10]	[0$\bar{1}$0]	[$\bar{1}$01]
[*uvw*]$_{Mo}$	[030]	[033]	[030]	[003]	[$\bar{3}$33]	[003]	[$\bar{3}$30]	[$\bar{3}$30]	[$\bar{3}$03]
d[*uvw*]$_{La2Ti2O7}$, nm	1.0059	1.42765	1.0095	1.42256	1.74227	1.0059	1.42256	2.46114	1.42256
d[*uvw*]$_{Mo}$, nm	0.95145	1.34555	0.95145	1.37145	1.66917	0.95145	1.68948	2.60113	1.68948
θ, °	0	0	0	0	0	0	0	0	0
δ	**5.53%**			**4.4%**			**14.4%**		

interface combined with the small size can effectively relieve the micro-elastic distortion around the reinforcing phase particles, and improve the macroscopic uniform plastic deformation ability of the material. However, the ductility of the alloy can be improved mainly by increasing the bonding force of the reinforced phase interface and changing the dislocations configuration to reduce the content of impurity elements.

Alloy strengthening during deformation is mainly due to the secondary phase particles and dynamic recrystallization affecting dislocations. Both recrystallization and deformation strengthening ultimately hinder the role of grain boundaries and dislocations. Because of the differences in secondary phase particles, the produced effect is different. In the Mo–La_2O_3 alloy, its strengthening single phase is La_2O_3. The mismatch between La_2O_3 and the matrix is less than TiC and TiO_2, so the strengthening effect is lower than in Mo–TiC. In addition, the amount of La_2O_3 in the matrix is too low, so the toughness reduction effect on the matrix is not obvious. In the Mo–TiC alloy, the main secondary phases are TiC and TiO_2. For TiC and TiO_2, the mismatch with the matrix is greater than for La_2O_3, so the strengthening effect is higher than Mo–La_2O_3, but the strength increases significantly, and, at the same time, plasticity decreases significantly.

For the Mo–TiC–La_2O_3 alloy, there are secondary phases of La_2O_3, TiC, TiO_2, and $La_2Ti_2O_7$. In the alloy, the micron particles are mainly $La_2Ti_2O_7$, while the secondary phases of the nanometer particles mainly include La_2O_3, TiC, and TiO_2, in which the amount of TiO_2 and La_2O_3 is small. However, TiC and TiO_2 have the highest average mismatch, which can effectively hinder and strengthen dislocations.

In addition to strengthening, rare earth oxides have a strong affinity with oxygen, and rare earth oxides have good thermal stability. Using rare earth metals to remove a small amount of oxygen in molybdenum alloy can reduce the content of impurity oxygen in the molybdenum matrix, reduce the brittleness of molybdenum alloys, and obtain an obvious toughening effect.

As shown in Fig. 8, there is a small amount of free oxygen on the surface of molybdenum powder. $La(NO_3)_3$ solution adheres to the surface of molybdenum powder and decomposes La^{3+} (Fig. 8a). La^{3+} adsorbs free oxygen on the surface of molybdenum powder nearby in Fig. 8b [11]. Not only the strength of molybdenum alloy is improved by the precipitation of secondary phase particles, but the plasticity of molybdenum alloy is improved by the reduction of impurity oxygen. The toughening effect is greater than the strengthening effect.

4. Conclusions

(1) The strength of alloys increases from Mo–La_2O_3 to Mo–TiC, to Mo–TiC–La_2O_3, and there is a variety of secondary phases at different scales in the Mo–TiC–La_2O_3 alloy. The grain size of the Mo–TiC–La_2O_3 alloy is the smallest, which is mainly formed by the multiple secondary phase pinning of nano-scale TiC, TiO_2, and La_2O_3.
(2) Mo–TiC–La_2O_3 alloy not only has a hardness of 368.1 ± 14.6 HV, the tensile strength of 1291.68 MPa, but also has a 6.59% elongation, with the best comprehensive properties.
(3) Mo–TiC–La_2O_3 alloy has a combined strengthening from nano-TiC, TiO_2, and $La_2Ti_2O_7$ phases. La_2O_3 plays a toughening role by purifying impurity oxygen at the grain boundary, and various secondary phases are coordinated.

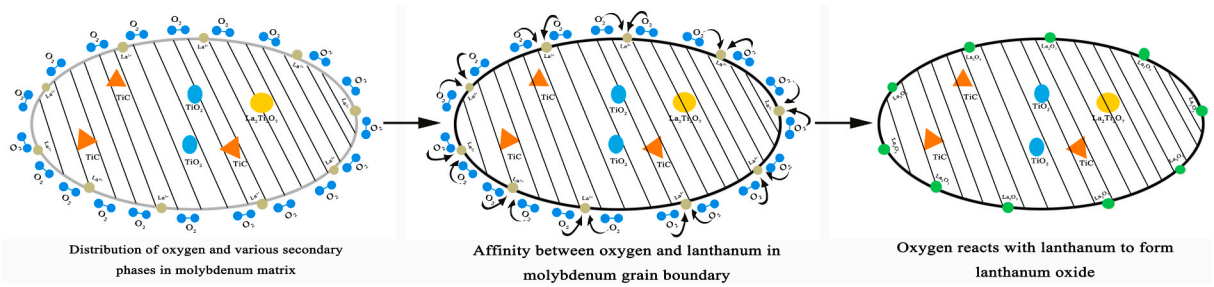

Fig. 8. Strengthening-toughening mechanism of rare earth elements in the molybdenum matrix.

CRediT authorship contribution statement

Bo-Liang Hu: performed sample preparation and Characterization, developed mechanics modelling and, Formal analysis, performed, Writing – original draft, and language polishing. **Jia-Yu Han:** performed sample preparation and Characterization. **Song-Wei Ge:** performed sample preparation and Characterization. **Xing-Jiang Hua:** performed data, Formal analysis. **Shi-Lei Li:** performed data, Formal analysis. **Hai-Rui Xing:** performed data, Formal analysis. **Kuai-She Wang:** Under, Supervision, developed mechanics modelling and, Formal analysis. **Ping Hu:** developed mechanics modelling and, Formal analysis, Under, Supervision. **Jing-Bo Fu:** performed sample preparation and Characterization. **Wen Zhang:** performed data, Formal analysis. **Alex A. Volinsky:** performed, Writing – original draft, and language polishing. **Ekaterina S. Marchenko:** performed, Writing – original draft, and language polishing. All authors read and contributed to the manuscript.

Declaration of competing interest

The authors declare that they have no known competing financial interests or personal relationships that could have appeared to influence the work reported in this paper.

Acknowledgments

This work was supported by the the National Natural Science Foundation of China (52104382). Postdoctoral Science Foundation of China (2021M693878), the Key R&D Program of Shaanxi Province, China (2021GY-209) Fok Ying Tung Education Foundation (171101), and the Youth Innovation Team of Shaanxi Universities (2019-2022). Service local special program of education department of Shaanxi province (21JC016). General Special Scientific Research Program of Shaanxi Provincial Department of Education (21JK0722), Top young talents project of “Special support program for high-level talents” in Shaanxi Province (2018-2023). Major scientific and technological projects in Shaanxi Province of China (2020ZDZX04-02-01). AV and EM acknowledge support by the Mega grant from the Government of the Russian Federation No. 220 of April 9, 2010 (Agreement No. 075-15-2021-612 of June 4, 2021).

References

[1] J. Fan, M. Lu, H. Cheng, J. Tian, B. Huang, Effect of alloying elements Ti, Zr on the property and microstructure of molybdenum, International Journal of Refractory Metals and Hard Materials 27 (1) (2009) 78–82.
[2] F. Jinglian, Q. Zhao, C. Huichao, T. Jiamin, C. Chuanggong, Effect of trace TiC/ZrC on property and microstructure of TZM alloy at room and high temperature, Rare metal materials and engineering 42 (4) (2013) 853–856.
[3] Y. Zhou, Y. Gao, S. Wei, K. Pan, Y. Hu, Preparation and characterization of Mo/Al_2O_3 composites, International Journal of Refractory Metals & Hard Materials 54 (2016) 186–195.
[4] P. Chen, M. Qin, C. Zheng, B. Jia, X. Qu, Solution combustion synthesis of nanosized WOx: characterization, mechanism and excellent photocatalytic properties, Rsc Advances 6 (86) (2016) 83101–83109.
[5] D. Wang, B. Yin, A. Sun, X. Li, C. Qi, B. Duan, Fabrication of Mo-Cu composite powders by heterogeneous precipitation and the sintering properties of the composite compacts, Journal of Alloys & Compounds 674 (2016) 347–352.
[6] Y. Fan, J. Wang, L. Wei, L. Xiang, M. Zhou, Studies on the pressed yttrium oxide-tungsten matrix as a possible dispenser cathode material, Materials Chemistry & Physics 149–150 (2015) 288–294.
[7] J. Wang, X. Zhang, W. Liu, Y. Cui, Y. Wang, M. Zhou, Recent progress on RE2O3-Mo/W emission materials, J Nanosci Nanotechnol 12 (8) (2012) 6499–6504.
[8] G.J. Zhang, Y.J. Sun, Z. Chao, J.F. Wei, J. Sun, Microstructure and mechanical properties of multi-components rare earth oxide-doped molybdenum alloys, Materials Science & Engineering A 483 (1) (2008) 350–352.
[9] J. Gan, Q. Gong, Y. Jiang, H. Chen, Y. Huang, K. Du, Y. Li, M. Zhao, F. Lin, D. Zhuang, Microstructure and high-temperature mechanical properties of second-phase enhanced Mo-La_2O_3-ZrC alloys post-treated by cross rolling, Journal of Alloys and Compounds 796 (2019) 167–175.
[10] R.E. Smallman, A.H.W. Ngan, Mechanical properties II-Strengthening and toughening, Physical Metallurgy & Advanced Materials Engineering (2007) 385–446.
[11] H.R. Xing, P. Hu, S.L. Li, Y.G. Zuo, J.Y. Han, X.J. Hua, K.S. Wang, F. Yang, P. F. Feng, T. Chang, Adsorption and diffusion of oxygen on metal surfaces studied by first-principle study: a review, Journal of Materials Science & Technology 62 (2021) 180–194.